Visible Light-driven, Nickel-doped Cobalt-oxides/hydroxides Actuators with High Stability

Kin Wa Kwan and Alfonso Hing Wan Ngan*

Department of Mechanical Engineering, The University of Hong Kong, Pokfulam Road, HKSAR

*Corresponding author email: kkwkwan@connect.hku.hk

KEYWORDS: Visible light-induced actuation, actuator, nickel hydroxide, cobalt hydroxide, doping

ABSTRACT: Material-based, light-driven actuators have been a recent research focus for the development of untethered, miniaturized devices and micro-robots. Recently introduced nickel hydroxide/oxyhydroxide ($Ni(OH)_2$/NiOOH) and cobalt oxides/hydroxides ($CoO_x(OH)_y$) are promising light-driven actuators as they exhibit large and rapid actuation response, and are inexpensive to fabricate by fast electrodeposition. However, as their actuation is due to the volume change accompanying the light-induced desorption of intercalated water in their turbostratic structures, their actuation reduces over time as crystallization takes place slowly which lowers the amount of water held. Here, we introduce nickel-doped cobalt oxides/hydroxides ($NiCoO_x(OH)_y$) actuator that exhibits similar turbostratic crystal structures and actuation magnitude as $CoO_x(OH)_y$, but with much slower crystallization and hence

significantly more stable actuation than $CoO_x(OH)_y$ or $Ni(OH)_2$/NiOOH. The new actuator exhibit much better applicability than the Co and Ni counterparts, and the present work shows that a stabilized turbostratic structure is a key for achieving high light-driven actuation in transition metal oxide/hydroxide actuators.

1. Introduction

Future robots rely on new functional materials,[1] and one of the key challenges for micro-scale robots is actuation methods commensurate with the micro length scale concerned that would be too small for conventional electromagnetic, hydraulic or pneumatic motors. Furthermore, for untethered robots or devices, remotely induced actuation is needed.[2-4] Therefore, light-driven compact actuating materials such as liquid crystal elastomers[5-10] and carbon-based[11-14] actuators have been introduced. Recently, actuators based on nickel hydroxide/oxyhydroxide ($Ni(OH)_2$/NiOOH)[15, 16] and cobalt oxides/hydroxides ($CoO_x(OH)_y$)[17] have been shown to be high-performing light-driven actuating materials with good potential for real applications. These materials can actuate with 0.5 – 1% intrinsic strain within seconds, by volume shrinkage accompanying the desorption of intercalated water in their turbostratic structure inducible by low-intensity visible light, which is less harmful to human than ultra-violet or infrared light. When electrodepositing the $Ni(OH)_2$/NiOOH or $CoO_x(OH)_y$ onto a thin passive substrate to form a bilayered structure, the 0.5 – 1% intrinsic strain can result in significant bending of the bilayer into curvatures as large as 1 mm^{-1}.[16, 17] The intrinsic actuation stress developed can be on the order of 60 MPa, which compares favorably with the best actuating materials known,[18] or is three orders of magnitude higher than the performance of human muscles.[18] Another advantage of $Ni(OH)_2$/NiOOH and $CoO_x(OH)_y$ is that they are inexpensive materials that can be fabricated by fast (< a few hours) electrodeposition or printed into arbitrary patterns on demand on different

substrates.[19] All these render $Ni(OH)_2$/NiOOH and $CoO_x(OH)_y$ desirable light-driven actuating materials with high potentials for application.

However, a major drawback of $Ni(OH)_2$/NiOOH and $CoO_x(OH)_y$ is that their actuation response deteriorates over time. This is because the actuation is caused by the volume change resulted from the water desorption from the materials when being illuminated, and the water was intercalated in the as-fabricated turbostratic structure. As such a structure is unstable and crystallizes slowly over time, the amount of intercalated water reduces, causing the deterioration of the actuation performance which greatly reduces the applicability of the actuators. In this study, we solve this critical problem by introducing a single-phase material of nickel-doped cobalt oxides/hydroxides ($NiCoO_x(OH)_y$) with significantly improved stability of the turbostratic structure and hence actuation performance. The fabrication, microstructural and actuation characterization, and the utilization of $NiCoO_x(OH)_y$ to design high-performing micro-robotic devices will be described here.

2. Experimental Section

2.1 Fabrication of Actuators. The bilayered actuator was fabricated by electrodepositing the active layer onto the passive substrate. The substrate was made of a nickel (Ni) film with a thin gold (Au) layer. First, an Ni film was electrodeposited on fluorine doped tin oxide (FTO) glass slides by a commercial Ni-plating kit (Caswell Inc.) at -15 mA/cm^2 for 5 min.[16] Then, a thin Au layers, which enhance the adhesion between the Ni film and the active layer, was electrodeposited on the Ni film in a bath of 1.7 M sodium sulfite (Na_2SO_3) and Oromerse SO Part B (Technic Inc.) in a volume ratio 9:1, at −0.1 mA/cm^2 for 30 min against a platinum (Pt) mesh. These result in a substrate thickness of 1.2 μm. Then, the actuator was made by

electrodepositing the active layer onto the Ni substrate. Five actuators were fabricated by the solutions specified in Table 1, which contain varying molarity of Ni^{2+} and Co^{2+} in the supporting electrolyte. The chemicals were purchased from Sigma-Aldrich and used without further purification, including 99.999% nickel sulfate heptahydrate ($NiSO_4 \cdot 7H_2O$, trace metals bases), ≥ 99.0% $NiSO_4 \cdot 7H_2O$ (purum p.a., crystallized), ≥ 99.0% cobalt sulfate heptahydrate ($CoSO_4 \cdot 7H_2O$, ReagentPlus®), sodium acetate (NaOAc) and sodium sulfate (Na_2SO_4) in puriss. p.a., anhydrous. Deionized (DI) water with a resistivity of ~18 megohms·cm was used to make all the solution baths and for rinsing. The electrodeposition was conducted with an anodic current density of 0.545 mA/cm^2 against saturated calomel reference electrode (SCE) and Pt mesh counter electrode in a three-electrode cell for 15 min at 40°C under vigorous stirring. The electrodeposited films measuring 22 mm by 2 mm were gray in color, and they together with the Ni substrates were then carefully peeled off the FTO glass. One end of the film actuators was adhered to copper tapes (3M) for clamping during the actuation tests.

Table 1. Solution bath compositions, thickness, electrodeposition rate and elastic modulus of the samples.

Sample / Solution bath components	Pure $Ni(OH)_2/NiOOH$	Normal $Ni(OH)_2/NiOOH$	$NiCoO_x(OH)_y$ (A) (Co : Ni = 0.027)	$NiCoO_x(OH)_y$- (B) (Co : Ni = 0.15)	$CoO_x(OH)_y$
$NiSO_4 \cdot 7H_2O$ 99.999% purity	0.13 M	/	/	/	/
$NiSO_4 \cdot 7H_2O$ ≥99% purity	/	0.13 M	0.063 M	0.054 M	/
$CoSO_4 \cdot 7H_2O$ ≥99% purity	/	/	0.0017 M	0.0083 M	0.05 M
NaOAc	0.13 M	0.13 M	0.065 M	0.063	0.05 M

Na_2SO_4	0.1 M	0.1 M	0.05 M	0.05	0.05 M
Thickness (μm)	~1	~1.2	~1.2	~1.2	~1.8
Electrodeposition rate (nm/min/M)	0.5	0.6	1.2	1.3	2.4
Elastic modulus (GPa)	13.8 ± 6.6	17.1 ± 5.7	17.6 ± 5.3	17.0 ± 5.6	16.9 ± 4.8

2.2 Materials Characterization. Cyclic voltammetry (CV) was performed by LK2006A electrochemical workstation (Lanlike), SEM and EDS by LEO 1530 FEG, TEM and SAED by FEI Tecnai $G^2$20 S-TWIN STEM, XRD by Rigaku SmartLab 9-kW X-ray diffractometer, 0.5° incidence angle, and XPS by Kratos Axis Ultra Spectrometer, monochromatic Al Kα source.

2.3 Actuation Tests. Actuation tests were performed in a tightly sealed transparent chamber at a temperature of 22°C to 24°C, at a relative humidity (RH) of 95% maintained by a wet sponge placed inside the chamber. The visible light source used to stimulate the samples was a xenon arc lamp LSH-X150 (Zolix Instruments Co. Ltd) with visible light filters (Shenzhen Fuzhe Technology Co. Ltd). The wavelength was measured by a spectrometer (HR2000 + CG, Ocean Optics) to be 400 to 700 nm, and the light intensity was measured by a TES11333 solar power meter (TES Electrical Electronic Corp.).

3. Results and Discussion

3.1 Materials Characterization. Two types of $NiCoO_x(OH)_y$ actuators ($NiCoO_x(OH)_y$ (A) and $NiCoO_x(OH)_y$ (B)) were made by the solution baths with Co : Ni molar ratio of 0.027 and 0.15, respectively. For comparison, $Ni(OH)_2$/NiOOH and $CoO_x(OH)_y$ were fabricated. Table 2 shows the corresponding element compositions measured by EDS. Pure $Ni(OH)_2$/NiOOH, fabricated using ultra-pure nickel sulfate of 99.999% purity, was found to be significantly

different from the normal $Ni(OH)_2$/NiOOH produced using ≥ 99% purity nickel sulfate as in previous studies.[15, 16, 20] While no Co was found in pure $Ni(OH)_2$/NiOOH, about 4 atomic % was found in normal $Ni(OH)_2$/NiOOH even the ≥ 99.0% $NiSO_4 \cdot 7H_2O$ used in the electrodeposition solution only contains a trace Co content of < 500 mg/kg as specified by the manufacturer. This shows that $Ni(OH)_2$/NiOOH is easily doped with a small amount of Co. Also, for $NiCoO_x(OH)_y$, small ratios of Co : Ni in the solution bath (0.027 or 0.15) would result in large ratios in the electrodeposited materials (1.62 or 3.56). All these suggest the preferential electrodeposition of $CoO_x(OH)_y$ against $Ni(OH)_2$/NiOOH, which may be caused by the lower energy required for the electrodeposition as indicated by the lower electrical potential applied to achieve the same current density. Also a a faster electrodeposition rate of $CoO_x(OH)_y$, estimated from the thickness divided by the electrodeposition time and the molarity of the Ni and/or Co (Table 1), is also found, potentially caused by the higher electrical conductivity of $CoO_x(OH)_y$.[21] As for $CoO_x(OH)_y$, no Ni was found by EDS.

Table 2. Atomic percentage of elements measured by EDS and the *d* spacing measured from SAED and XRD.

Sample	Pure $Ni(OH)_2$/NiOOH	Normal $Ni(OH)_2$/NiOOH	$NiCoO_x(OH)_y$ (A)	$NiCoO_x(OH)_y$ (B)	$CoO_x(OH)_y$
Element	Atomic %				
O	49.17	52.85	57.35	65.90	43.56
Co	/	4.43	23.53	24.43	54.16
Ni	37.51	33.05	14.52	6.85	/
Au	13.32	9.67	4.60	2.81	2.28
Total:	100.00	100.00	100.00	100.00	100.00

Co : Ni ratio	/	0.13	1.62	3.56	/
d spacing (Å) by SAED	2.32	2.44	2.24	2.35	2.42
	1.43	1.51	1.45	1.46	1.47
d spacing (Å) by XRD	9.6	4.8	2.4	2.4	2.4
	4.8				
	3.2	2.4	1.4	1.4	1.4
	2.4				
	1.8	1.4			
	1.4				

The morphologies observed under SEM (Fig. 1a) are similar for all samples, except that pure $Ni(OH)_2$/NiOOH is significantly more porous than the others. This is also found in TEM imaging (Fig. 1b). Under closer examination in SEM, normal $Ni(OH)_2$/NiOOH appears to be denser than the pure counterpart; and with the increase in Co content, the roughness of the surface decreases while the density increases, and perpendicular cracks are found. As the material contracts under low humidity,[16] it will contract in the vacuum chamber of the SEM. So, the denser and thicker the active layer is, the wider the perpendicular cracks observed. Dispersed rings are observed in selected-area electron diffraction (SAED) in the TEM (Fig. 1c), showing that the samples are not well-crystalline, in agreement with the turbostratic structures reported beforehand.[15, 16, 20] The measurable *d* spacings of pure and normal $Ni(OH)_2$/NiOOH in Table 2 roughly match the (002) and (110) planes of β-NiOOH or the (102) and (110) of γ-NiOOH.[22] For $CoO_x(OH)_y$, the *d* spacings can be related to the (111) and $(11\bar{3})$ of $Co(OH)_2$, $(10\bar{1}2)$ and $(2\bar{1}\bar{1}0)$ of CoOOH and (311) and (440) of Co_3O_4, and therefore it is identified as the oxides/hydroxides

of Co.[17] For $NiCoO_x(OH)_y$'s, the measurable *d* spacings are similar to $Ni(OH)_2$/NiOOH and $CoO_x(OH)_y$.

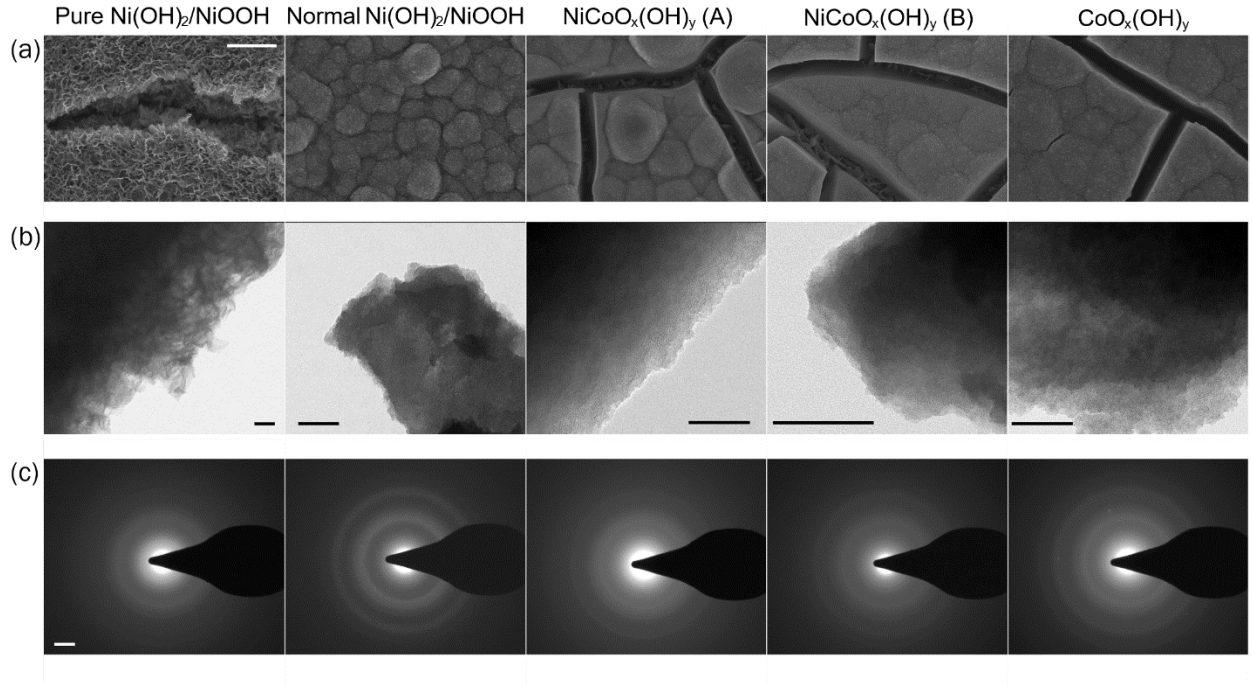

Figure 1. (a) SEM (scale bar: 1 μm), (b) TEM (scale bar: 100 nm) and (c) SAED (scale bar: 2 nm^{-1}) of the samples.

As diffraction peaks of turbostratic structures are intrinsically weak, glazing angle XRD was carried out to reduce the signals from the underlying layers. In Fig. 2a, the weak diffractions of pure and normal $Ni(OH)_2$/NiOOH electrodeposited on Ni substrate on FTO are shown, with measurable *d* spacings summarized in Table 2. Peaks at 2θ = 9.2° and 28.3° cannot be found in normal $Ni(OH)_2$/NiOOH and the one at 18.6° is much sharper for the pure one. This suggests a different phase with a higher crystallinity was electrodeposited from the pure solution. The planes corresponding to 2θ = 9.2° (*d* = 9.6 Å) and 28.3° (*d* = 3.2 Å) should be the basal plane of α-$Ni(OH)_2$[23] and (006) of γ-NiOOH,[22] while the one at 2θ = 18.6° corresponds to (001) of β-$Ni(OH)_2$[24] or β-NiOOH.[22] For both types of $Ni(OH)_2$/NiOOH, 2θ = 37.7° (*d* = 2.4 Å) and 2θ =

66.7° (d = 1.4 Å) match the SAED results – (002) and (110) planes of β-NiOOH or (102) and (110) of γ-NiOOH[22]) and 2θ = 61.6° matches (111) of β-$Ni(OH)_2$[24] or (301) of α-$Ni(OH)_2$.[24] These suggest that both $Ni(OH)_2$/NiOOH's are likely to be composed of a mixture of different phases of hydroxide and oxyhydroxide.

As $NiCoO_x(OH)_y$ and $CoO_x(OH)_y$ layers would easily delaminate from Ni substrates, possibly due to a weaker adhesive strength on Ni, XRD was performed on Au coated Ni ($Ni(OH)_2$/NiOOH's were also tested for comparison). As shown in Fig. 2b, the XRD curves for $NiCoO_x(OH)_y$ and $CoO_x(OH)_y$ are similar, with a small Au peak observed at 2θ = 38.4°, 44.6°, 64.8° and 77.7° for $NiCoO_x(OH)_y$ (A), and 38.2° and 44.5° for $CoO_x(OH)_y$. Although overlapped with the Au peaks, magnified curves (Fig. 2c) show broad peaks at about 38° and 66°, giving d = 2.4 and 1.4 Å that match with the SAED. As no reflections for hydrotalcite-like layered double hydroxide (LDH) can be found for $NiCoO_x(OH)_y$, these samples are identified as exhibiting the same phase constitution and structure as $CoO_x(OH)_y$, albeit that the significant amount of Ni found in EDS. Therefore, $NiCoO_x(OH)_y$ is identified as Ni-doped Co oxides/hydroxides. Recalling that a very low Co : Ni molar ratio of 0.027 or 0.15 in the solution bath can lead to a much higher Co : Ni ratio of 1.62 or 3.56 in the deposited product, the observed persistence of the $CoO_x(OH)_y$ phase structure in the co-deposited $NiCoO_x(OH)_y$ samples indicates once again the much higher stability of $CoO_x(OH)_y$ relative to $Ni(OH)_2$/NiOOH. The XRD curves of $CoO_x(OH)_y$ and $NiCoO_x(OH)_y$'s have much weaker peaks, but with higher background signals, than $Ni(OH)_2$/NiOOH's, indicating that the former materials have higher turbostraticity than the latter. Besides, normal $Ni(OH)_2$/NiOOH containing ~4% Co exhibits broader and weaker diffraction peaks than the pure one, which indicates that Co doping can also increase the turbostraticity in $Ni(OH)_2$/NiOOH structure.

Cyclic voltammetry (CV) in 1 M sodium hydroxide (NaOH) (Fig. 2d) reveal that the peak currents for the redox reaction $Ni(OH)_2 \leftrightarrow NiOOH$ in normal $Ni(OH)_2$/NiOOH are lower than the pure counterpart, likely due to the decrease in porosity (observed from SEM) and hence surface area.[25] The CV's for $NiCoO_x(OH)_y$'s and $CoO_x(OH)_y$ are flat without exhibiting the same redox peaks as $Ni(OH)_2$/NiOOH. These once again indicate that $NiCoO_x(OH)_y$ is electrochemically more similar to $CoO_x(OH)_y$ than to $Ni(OH)_2$/NiOOH, although the detailed differences in the CV between $NiCoO_x(OH)_y$ and $CoO_x(OH)_y$ reflect their difference in chemical compositions. Lastly, XPS on normal $Ni(OH)_2$/NiOOH and $NiCoO_x(OH)_y$ (A) (Fig. 2e, f) confirms the EDS result on the Co content, where the ratio of Co : Ni calculated is 0.08 for normal $Ni(OH)_2$/NiOOH and 1.6 for $NiCoO_x(OH)_y$ (A). The double peaks for Ni 2p 3/2 at around 854 eV indicate the presence of Ni^{2+} and Ni^{3+} in the samples,[26] and that of Co 2p 3/2 should correspond to Co^{2+} and Co^{3+}.[27]

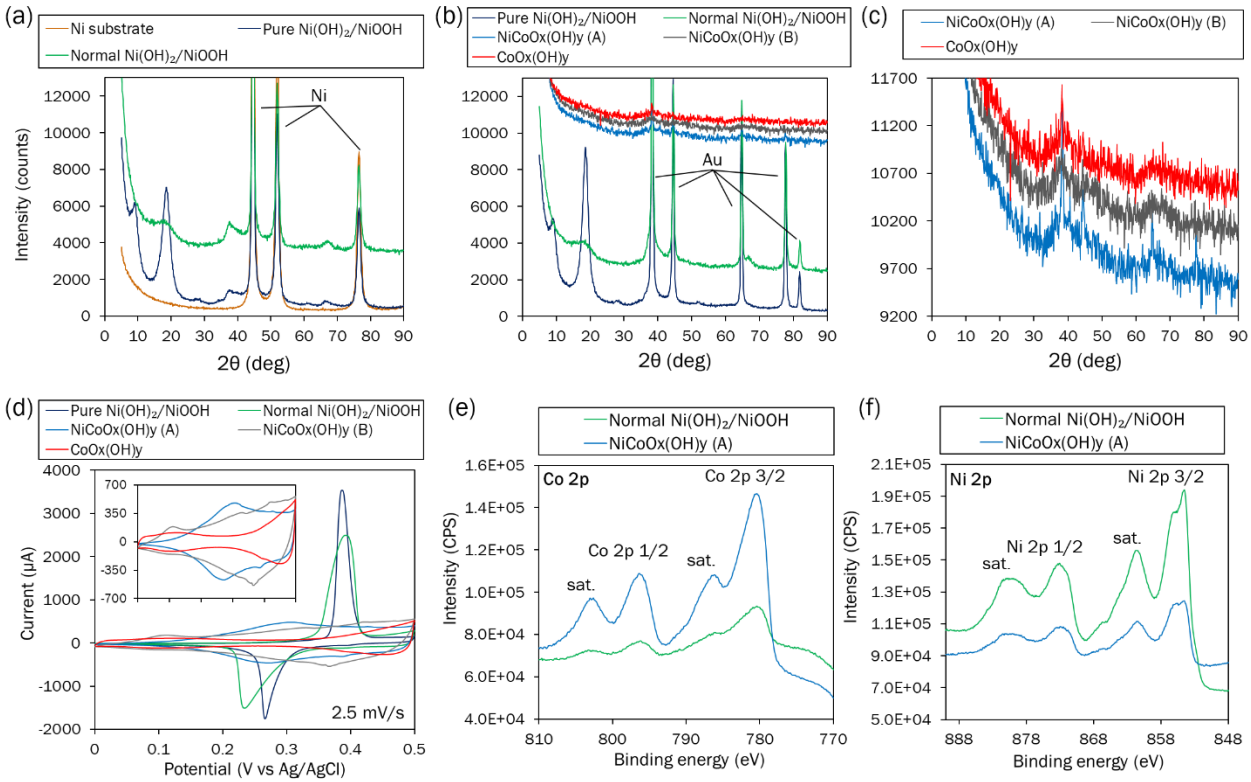

Figure 2. XRD on samples with (a) Ni substrate and (b) Au substrate. (c) Magnified view of (b) showing the broad peaks of $NiCoO_x(OH)_y$ and $CoO_x(OH)_y$. (d) CV of the samples in 1 M NaOH. XPS for (e) Co 2p and (f) Ni 2p photoelectrons.

3.2 Actuation Tests. Due to the turbostratic structure, water molecules in air moisture can adsorb on the surface and intercalate between the basal planes of the crystal of the actuating materials.[23, 28, 29] Under visible light illumination, the water molecules will be de-intercalated and desorbed from the actuating layer ($NiCoO_x(OH)_y$, $Ni(OH)_2$/NiOOH or $CoO_x(OH)_y$) potentially caused by a photothermal effect,[17] which results in a volume contraction and bending of the whole actuator because of the constraint of the passive substrate. The actuators will recover when the illumination is switched off, as water molecules adsorb and intercalate back to the active materials. Due to the high aspect ratio of the samples (length : thickness ≈ 10,000), they may curl and twist into loops. As shown in Fig. 3a and Video S1, pure $Ni(OH)_2$/NiOOH has the weakest actuation (quantified by curvature κ and intrinsic actuation strain), with the actuation increases with the Co content generally. This indicates that a higher actuation performance is related to a higher density and turbostraticity of the structure as the Co content increases as observed from SEM and XRD, and these would lead to higher elastic modulus of the active layer and higher amount of water intercalation.

For $CoO_x(OH)_y$, the actuation at low light intensities (10 and 20 mW/cm^2) is relatively small, but at 50 mW/cm^2, κ becomes very high as shown in Fig. 3b. This indicates that $CoO_x(OH)_y$ is less sensitive to low intensity light than normal $Ni(OH)_2$/NiOOH and $NiCoO_x(OH)_y$ which may be due to its higher thickness than the others (~1.8 μm vs ~1.2 μm). As the actuation depends on diffusion of water from the interior to the surface of the active material,[17] a higher thickness may require a higher light intensity to fully trigger the actuation. Fig. 3c shows the intrinsic actuation

strain calculated from an equation published previously,[15] which is proportional to κ and roughly inversely proportional to the thickness of the active layer (thickness and elastic modulus of the substrate are the same for all samples, namely, 1.2 μm and 220 GPa respectively). In terms of strain, $NiCoO_x(OH)_y$ (B) exerts the highest strain, followed by $NiCoO_x(OH)_y$ (A). The strain of $CoO_x(OH)_y$ is higher than $NiCoO_x(OH)_y$ (A) and normal $Ni(OH)_2$/NiOOH at 50 mW/cm^2, but is lower at 10 and 20 mW/cm^2. This shows that the presence of Ni increases the tendency of light-induced water desorption. Note that the strain calculation does not consider the presence of cracks as their consideration will greatly increase the complexity of the model. Nevertheless, assuming a perfect structure should slightly underestimate the strain, which should still serve as a good indicator for the actuation performance. From the higher tendency of water de-intercalation and the higher turbostraticity observed, we can conclude that there is a synergistic effect of Co and Ni in the actuating material which gives better actuation magnitude than the compositions containing pure Ni or Co. For a more detailed mechanism, future work is needed to closely investigate the bonding and structure of the materials.

As mentioned in the introduction section, the stability of the actuation is an important concern for real life applications. To examine this, two tests were performed. In the first one, the actuation was compared before and after 3 days of idling to detect any degradation. The second one tests for the repeatability of the actuation over 5000 cycles. From Fig. 3d, it is found that $NiCoO_x(OH)_y$ (A) and $NiCoO_x(OH)_y$ (B) exhibit the lowest drop in actuation curvature κ, namely, only less than 10% drop while the others exhibit drops in κ by more than 20%. Their recovery speed (the speed for the actuator to return to the original shape when the light is switched off) also shows small decrease of about 10 m^{-1}s^{-1}, in contrary to the more than 50 m^{-1}s^{-1} for $CoO_x(OH)_y$ and normal $Ni(OH)_2$/NiOOH. From Video S2, $NiCoO_x(OH)_y$ (A) has a slightly

better idling stability than $NiCoO_x(OH)_y$ (B). Also, $NiCoO_x(OH)_y$ (A) shows good cyclic stability as shown in Fig. 3e over 5000 cycles (Video S3, which also shows the actuation with 100 h idling after the cycle test), which is also achievable by $Ni(OH)_2$/NiOOH, and marginally by $CoO_x(OH)_y$ as reported previously.[16, 17] Examining the cross section of $NiCoO_x(OH)_y$ (A) before and after the cycle test under SEM (Fig. 3f) reveals little change in the structure, indicating that there is no deterioration or delamination between the active and passive layers after repeated actuation. Note that the large cracks of the active materials observed under SEM (Fig. 1a and 3f) are likely caused by the vacuum of the microscope chamber that would severely dry and contract the materials. Smaller cracks are expected under normal environment due to the brittle nature of the materials. If the light intensity is low or the illumination duration is short, there would not be serious cracks or delamination observable from naked eye that would affect the actuation. Besides, similar to $Ni(OH)_2$/NiOOH, $NiCoO_x(OH)_y$ and $CoO_x(OH)_y$ can be actuated electrochemically in NaOH electrolyte (Video S4). It can be seen that $NiCoO_x(OH)_y$'s also have better electrochemical actuation, and as this study focuses on light actuation, the behavior of electrochemical actuation will not be reported here.

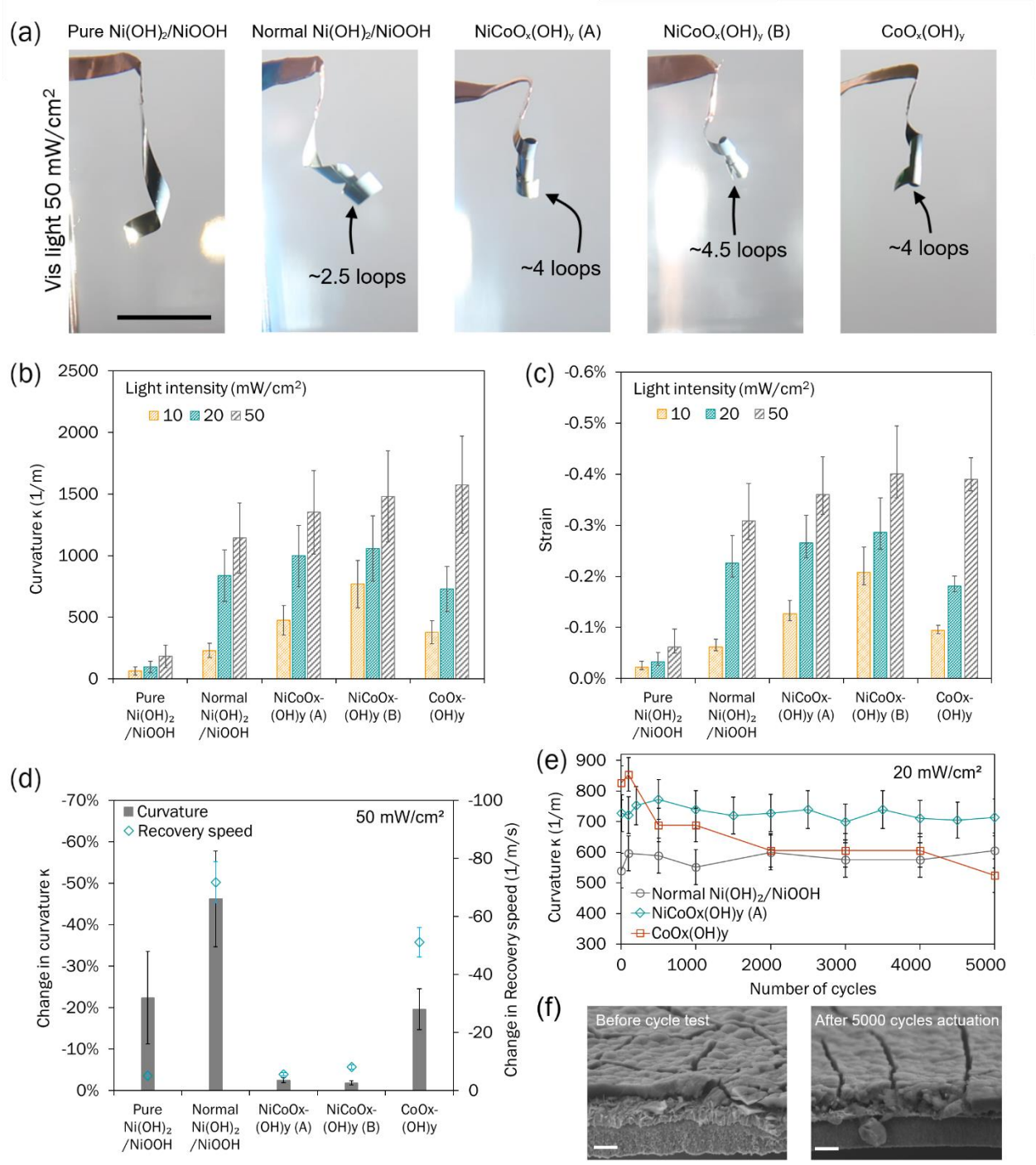

Figure 3. (a) Photos of visible light actuations at 50 mW/cm^2 (scale bar: 10 mm). (b) Curvature κ and (c) actuation strain at various light intensity. (d) Change of curvature κ and recovery speed after 3 days of idling. (e) Repeatability test over 5000 of cycles, with the data of

$Ni(OH)_2$/NiOOH and $CoO_x(OH)_y$ replotted from reference 16 and 17 respectively. (Error bars for (b) to (e): estimated measurement errors.) (f) SEM images on cross section of $NiCoO_x(OH)_y$ (A) actuator before and after 5000 cycles of actuation (scale bar: 1μm).

To investigate the decrease in actuation, XRD was performed on the samples after being put into a humid environment (RH = 95%) for 10 days (pure $Ni(OH)_2$/NiOOH is not examined due to the low actuation). Replotting the XRD in Fig. 2a for comparison, Fig. 4a shows the change in XRD after 10 days. The peak of normal $Ni(OH)_2$/NiOOH at 2θ = 19° sharpens slightly, and reduction occurred as indicated in the shift at 2θ = 60.9°.[16] As for $NiCoO_x(OH)_y$ (A), $NiCoO_x(OH)_y$ (B) and $CoO_x(OH)_y$, a peak at 19° appears after 10 days. The peaks for Au also sharpen, which may be caused by the slight delamination of the sample from FTO at some spots after 10 days, so that more X-ray can be diffracted from Au. Among these 3 samples, the change in $NiCoO_x(OH)_y$ (A) is the least, explaining the best stability found in Fig. 3d, 3e and Video S3, S4. The increase in stability may be caused by the higher bond strength of the Co that makes it more thermally stable in water.[30] Also, Co can enhance the electrostatic attraction between the layered $Ni(OH)_2$ host and the anions in the inter-layer spacing, so as to increase the stability against crystallization in alkaline medium.[31] Although the actuators in this study were not operated in water or alkaline media, the moisture in air may provide a similar environment that tends to crystallize the turbostratic actuating materials. Further study is needed to investigate the detailed mechanism of the stability effect.

The above results show that $NiCoO_x(OH)_y$ (A) is a good actuator for real applications. Here, we show two demonstrations in which the active layer is selectively electrodeposited to form simple kirigami actuators. Figure 4b shows the schematic diagram of fabricating a kirigami with 4 actuating hinges. First, a substrate with two cutting lines was made by masking the FTO glass

with a permanent marker pen as shown. Then, after electrodepositing the Ni-Au substrate, selective deposition of $NiCoO_x(OH)_y$ (A) was achieved by masking the substrate to leave open 4 rectangular areas as shown. Released from the FTO by peeling, the actuator can perform self-folding as shown in Fig. 4c under illumination of 50 mW/cm^2 visible light and weightlift an object of 40 mg by 5.5 mm (Fig. 4d and Video S5). Figure 4e shows another example of kirigami, which is a pinwheel-like structure with the petals curled under illumination (Video S5).

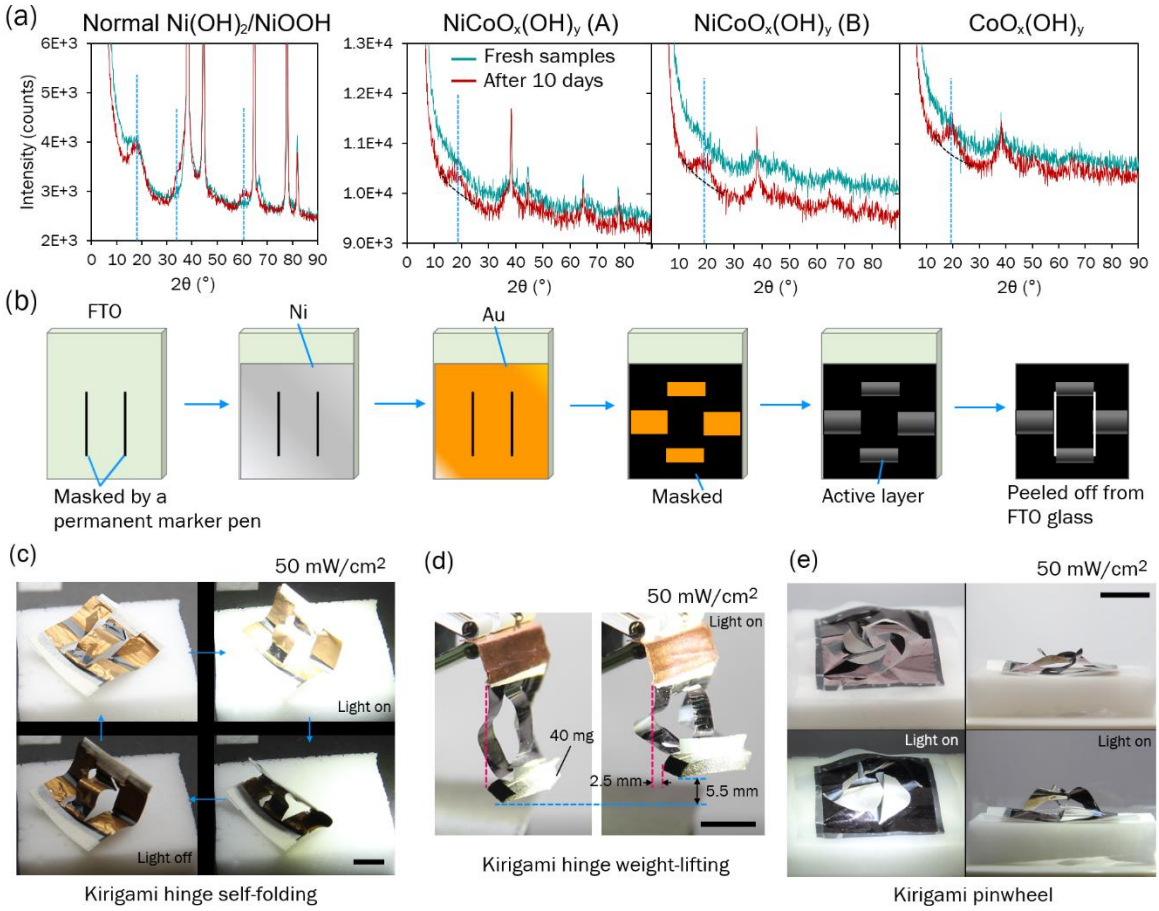

Figure 4. (a) XRD on fresh samples (replotted from Fig. 2a) and after 10 days of idling in a humid environment. (b) Schematic diagram of fabrication of a kirigami actuator. Photos of actuation of a kirigami actuating hinge performing (c) self-folding and (d) weightlifting, and (e) a kirigami pinwheel (scale bar: 10 mm).

From the actuation tests, it is clear that $NiCoO_x(OH)_y$, which is Ni-doped and isostructural with $CoO_x(OH)_y$ (Fig. 2c), exhibits high actuation strains comparable to pure $CoO_x(OH)_y$ (Fig. 3b,c), and yet much more stable (Fig. 3d). Also, normal $Ni(OH)_2$/NiOOH, a slightly Co-doped material exhibits better actuation than the pure counterpart (Fig. 3b,c). In the field of battery and catalyst research, Ni and Co are often doped into the oxide/hydroxide/oxyhydroxide of the other to improve the performance,[30-38] and the present study shows that not only the electrochemical activity, but the light-driven actuation behavior can also be enhanced by doping. This study shows a remarkable improvement in actuation stability from $NiCoO_x(OH)_y$, achieved by the stabilized turbostratic structure that is resistant to crystallization and therefore immune from degradation in actuation performance. The present results also imply new actuators with better performance can be developed from doping of other metals such as Al, Cu, Fe, Mn or Zn.

4. Conclusion

In conclusion, visible light-driven nickel-doped cobalt oxides/hydroxides ($NiCoO_x(OH)_y$) actuators are developed, which show high actuation performance in terms of magnitude and stability. Structural study shows that the higher actuation magnitude is caused by the higher turbostraticity and density, and the higher stability is due to a lower rate of crystallization. The $NiCoO_x(OH)_y$ actuators thus show promising actuation performance for future robotics applications.

ASSOCIATED CONTENT

Supporting Information

Video S1: Visible light actuation

Video S2: Idling stability test

Video S3: Cycle test

Video S4: Electrochemical actuation

Video S5: Kirigami demos

AUTHOR INFORMATION

Corresponding Author

Kin Wa Kwan – Department of Mechanical Engineering, The University of Hong Kong, Pokfulam Road, Hong Kong

Author Contributions

The manuscript was written through contributions of all authors. All authors have given approval to the final version of the manuscript. KW Kwan: Conceptualization, Investigation: performing experiments, data collection and analysis, Writing: original draft, review & editing. AHW Ngan: Supervision, Investigation: analysis, Writing: review & editing, Funding acquisition.

Funding Sources

This work was funded by a grant from the Research Grants Council (project no. 17206114) of the Hong Kong Special Administrative Region and the Kingboard Endowed Professorship in Materials Engineering.

Notes

The authors declare no competing financial interest.

ACKNOWLEDGMENT

The authors thank F. Y. F. Chan for the operation of TEM**.**

REFERENCES

1. Yang, G.-Z.; Bellingham, J.; Dupont, P. E.; Fischer, P.; Floridi, L.; Full, R.; Jacobstein, N.; Kumar, V.; McNutt, M.; Merrifield, R., The Grand Challenges of Science Robotics. *Sci. Robot.* **2018,** *3* (14), eaar7650.

2. Kim, Y.; Yuk, H.; Zhao, R.; Chester, S. A.; Zhao, X., Printing Ferromagnetic Domains for Untethered Fast-Transforming Soft Materials. *Nature* **2018,** *558* (7709), 274.

3. Jafferis, N. T.; Helbling, E. F.; Karpelson, M.; Wood, R. J., Untethered Flight of an Insect-Sized Flapping-Wing Microscale Aerial Vehicle. *Nature* **2019,** *570* (7762), 491-495.

4. Miyashita, S.; Guitron, S.; Ludersdorfer, M.; Sung, C. R.; Rus, D. In *An Untethered Miniature Origami Robot That Self-Folds, Walks, Swims, and Degrades*, 2015 IEEE International Conference on Robotics and Automation (ICRA), IEEE: 2015; pp 1490-1496.

5. van Oosten, C. L.; Corbett, D.; Davies, D.; Warner, M.; Bastiaansen, C. W.; Broer, D. J., Bending Dynamics and Directionality Reversal in Liquid Crystal Network Photoactuators. *Macromolecules* **2008,** *41* (22), 8592-8596.

6. Van Oosten, C. L.; Bastiaansen, C. W.; Broer, D. J., Printed Artificial Cilia from Liquid-Crystal Network Actuators Modularly Driven by Light. *Nat. Mater.* **2009,** *8* (8), 677.

7. Serak, S.; Tabiryan, N.; Vergara, R.; White, T. J.; Vaia, R. A.; Bunning, T. J., Liquid Crystalline Polymer Cantilever Oscillators Fueled by Light. *Soft Matter* **2010,** *6* (4), 779-783.

8. Wu, W.; Yao, L.; Yang, T.; Yin, R.; Li, F.; Yu, Y., Nir-Light-Induced Deformation of Cross-Linked Liquid-Crystal Polymers Using Upconversion Nanophosphors. *J. Am. Chem. Soc.* **2011,** *133* (40), 15810-15813.

9. Cheng, Z.; Wang, T.; Li, X.; Zhang, Y.; Yu, H., Nir–Vis–Uv Light-Responsive Actuator Films of Polymer-Dispersed Liquid Crystal/Graphene Oxide Nanocomposites. *ACS Appl. Mater. Interfaces* **2015,** *7* (49), 27494-27501.

10. White, T. J.; Broer, D. J., Programmable and Adaptive Mechanics with Liquid Crystal Polymer Networks and Elastomers. *Nat. Mater.* **2015,** *14* (11), 1087.

11. Wang, E.; Desai, M. S.; Lee, S.-W., Light-Controlled Graphene-Elastin Composite Hydrogel Actuators. *Nano Lett.* **2013,** *13* (6), 2826-2830.

12. Ji, M.; Jiang, N.; Chang, J.; Sun, J., Near-Infrared Light-Driven, Highly Efficient Bilayer Actuators Based on Polydopamine-Modified Reduced Graphene Oxide. *Adv. Funct. Mater.* **2014,** *24* (34), 5412-5419.

13. Mu, J.; Hou, C.; Wang, H.; Li, Y.; Zhang, Q.; Zhu, M., Origami-Inspired Active Graphene-Based Paper for Programmable Instant Self-Folding Walking Devices. *Sci. Adv.* **2015,** *1* (10), e1500533.

14. Han, B.; Zhang, Y. L.; Zhu, L.; Li, Y.; Ma, Z. C.; Liu, Y. Q.; Zhang, X. L.; Cao, X. W.; Chen, Q. D.; Qiu, C. W., Plasmonic-Assisted Graphene Oxide Artificial Muscles. *Adv. Mater.* **2019,** *31* (5), 1806386.

15. Kwan, K.-W.; Hau, N.-Y.; Feng, S.-P.; Ngan, A. H.-W., Electrochemical Actuation of Nickel Hydroxide/Oxyhydroxide at Sub-Volt Voltages. *Sensors and Actuators B: Chemical* **2017,** *248*, 657-664.

16. Kwan, K.; Li, S.; Hau, N.; Li, W.-D.; Feng, S.; Ngan, A. H., Light-Stimulated Actuators Based on Nickel Hydroxide-Oxyhydroxide. *Sci. Robot.* **2018,** *3* (18), eaat4051.

17. Kwan, K. W.; Ngan, A. H. W., A High-Performing, Visible-Light-Driven Actuating Material Responsive to Ultralow Light Intensities. *Advanced Materials Technologies* **2019,** *0* (0), 1900746.

18. Madden, J. D.; Vandesteeg, N. A.; Anquetil, P. A.; Madden, P. G.; Takshi, A.; Pytel, R. Z.; Lafontaine, S. R.; Wieringa, P. A.; Hunter, I. W., Artificial Muscle Technology: Physical Principles and Naval Prospects. *IEEE Journal of oceanic engineering* **2004,** *29* (3), 706-728.

19. Wu, R.; Kwan, K. W.; Ma, W.; Wang, P.; Ngan, A. H. W., Self-Actuating Origamis Realized by Independently Printable and Controllable Stimuli-Responsive Creases. *Applied Materials Today* **2020,** *Accepted*.

20. Kwan, K. W.; Xie, D.; Zhang, R.; Shan, Z.; Ngan, A. H., Electron-Beam Induced Water Removal, Phase Change, and Crystallization of Anodic-Electrodeposited Turbostratic Nickel Hydroxide-Oxyhydroxide. *physica status solidi (a)* **2018,** *215* (23), 1800623.

21. Tench, D.; Warren, L. F., Electrodeposition of Conducting Transition Metal Oxide/Hydroxide Films from Aqueous Solution. *J. Electrochem. Soc.* **1983,** *130* (4), 869.

22. Singh, D., Characteristics and Effects of Γ-Niooh on Cell Performance and a Method to Quantify It in Nickel Electrodes. *J. Electrochem. Soc.* **1998,** *145* (1), 116-120.

23. Faure, C.; Delmas, C.; Fouassier, M., Characterization of a Turbostratic A-Nickel Hydroxide Quantitatively Obtained from an Niso4 Solution. *J. Power Sources* **1991,** *35* (3), 279-290.

24. Hall, D. S.; Lockwood, D. J.; Bock, C.; MacDougall, B. R., Nickel Hydroxides and Related Materials: A Review of Their Structures, Synthesis and Properties. *Proceedings of the Royal Society A: Mathematical, Physical and Engineering Sciences* **2015,** *471* (2174), 20140792.

25. Menshykau, D.; Compton, R. G., The Influence of Electrode Porosity on Diffusional Cyclic Voltammetry. *Electroanalysis: An International Journal Devoted to Fundamental and Practical Aspects of Electroanalysis* **2008,** *20* (22), 2387-2394.

26. Jia, H.; Zhu, W.; Xu, Z.; Nie, X.; Liu, T.; Gao, L.; Zhao, J., Precursor Effects on Structural Ordering and Electrochemical Performances of Ni-Rich Layered Lini0. 8co0. 2o2 Cathode Materials for High-Rate Lithium Ion Batteries. *Electrochim. Acta* **2018,** *266*, 7-16.

27. Han, Y.; Axnanda, S.; Crumlin, E. J.; Chang, R.; Mao, B.; Hussain, Z.; Ross, P. N.; Li, Y.; Liu, Z., Observing the Electrochemical Oxidation of Co Metal at the Solid/Liquid Interface Using Ambient Pressure X-Ray Photoelectron Spectroscopy. *The Journal of Physical Chemistry B* **2017,** *122* (2), 666-671.

28. Oliva, P.; Leonardi, J.; Laurent, J.; Delmas, C.; Braconnier, J.; Figlarz, M.; Fievet, F.; Guibert, A. d., Review of the Structure and the Electrochemistry of Nickel Hydroxides and Oxy-Hydroxides. *J. Power Sources* **1982,** *8*, 229-255.

29. Jahangiri, S.; Mosey, N. J., Molecular Structure and Interactions of Water Intercalated in Nickel Hydroxide. *PCCP* **2018,** *20* (16), 11444-11453.

30. Faure, C.; Delmas, C.; Willmann, P., Preparation and Characterization of Cobalt-Substituted A-Nickel Hydroxide Stable in Koh Medium Part Ii. A-Hydroxide with a Turbostratic Structure. *J. Power Sources* **1991,** *35* (3), 263-277.

31. Huang, H.; Guo, Y.; Cheng, Y., Ultrastable A Phase Nickel Hydroxide as Energy Storage Materials for Alkaline Secondary Batteries. *Appl. Surf. Sci.* **2018,** *435*, 635-640.

32. Faure, C.; Delmas, C.; Willmann, P., Electrochemical Behavior of A-Cobalted Nickel Hydroxide Electrodes. *J. Power Sources* **1991,** *36* (4), 497-506.

33. Faure, C.; Delmas, C.; Fouassier, M.; Willmann, P., Preparation and Characterization of Cobalt-Substituted A-Nickel Hydroxides Stable in Koh Medium Part I. A′-Hydroxide with an Ordered Packing. *J. Power Sources* **1991,** *35* (3), 249-261.

34. Delmas, C.; Faure, C.; Borthomieu, Y., The Effect of Cobalt on the Chemical and Electrochemical Behaviour of the Nickel Hydroxide Electrode. *Materials Science and Engineering: B* **1992,** *13* (2), 89-96.

35. Kim, M. S.; Kim, K. B., A Study on the Phase Transformation of Electrochemically Precipitated Nickel Hydroxides Using an Electrochemical Quartz Crystal Microbalance. *J. Electrochem. Soc.* **1998,** *145* (2), 507.

36. Nethravathi, C.; Ravishankar, N.; Shivakumara, C.; Rajamathi, M., Nanocomposites of A-Hydroxides of Nickel and Cobalt by Delamination and Co-Stacking: Enhanced Stability of A-Motifs in Alkaline Medium and Electrochemical Behaviour. *J. Power Sources* **2007,** *172* (2), 970-974.

37. Martins, P. R.; Parussulo, A. L. A.; Toma, S. H.; Rocha, M. A.; Toma, H. E.; Araki, K., Highly Stabilized Alpha-Nico (Oh) 2 Nanomaterials for High Performance Device Application. *J. Power Sources* **2012,** *218*, 1-4.

38. Martins, P. R.; Ferreira, L. M. C.; Araki, K.; Angnes, L., Influence of Cobalt Content on Nanostructured Alpha-Phase-Nickel Hydroxide Modified Electrodes for Electrocatalytic Oxidation of Isoniazid. *Sensors and Actuators B: Chemical* **2014,** *192*, 601-606.